Int. J. Solids Structures Vol. 29, No. 12, pp. 1549–1565, 1992
Printed in Great Britain.

0020–7683/92 $5.00 + .00

ELASTIC WAVE SCATTERING BY RECTANGULAR CRACKS

LINGWEI GUAN
School of Civil and Structural Engineering, Nanyang Technological University, Nanyang Avenue, Singapore 2263

and

ANDREW NORRIS
Department of Mechanical and Aerospace Engineering, Rutgers University, Piscataway, NJ 08855-0909, U.S.A.

(*Received* 18 *April* 1991; *in revised form* 2 *October* 1991)

Abstract—Three coupled integral equations are formulated for the direct problem of scattering of obliquely incident longitudinal plane waves from a rectangular crack. Chebyshev functions are used to expand the unknown crack opening displacements and to convert the integral equations into an infinite linear system of simultaneous equations which are solved by numerical truncation. The static and dynamic stress intensity factors for a square crack under normal incidence show very good agreement with all data reported by other researchers. For a rectangular crack, the ratio between the two local maxima of Mode I stress intensity factors is found to be the square root of the aspect ratio. A Rayleigh wave membrane analogy is used to explain the appearance of peaks in the dynamic responses. All the results for cracks under oblique incidence are new, as well as the scattered far-fields and their long wavelength or quasi-static limits. The asymptotes of the scattering cross-sections in the high frequency region are found to vary linearly with the cosines of the incident angles, and a corner effect is observed in the scattering patterns for moderately high frequencies.

1. INTRODUCTION

The study of elastic wave scattering by cracks is of some importance in the field of ultrasonic non-destructive testing and evaluation. However, to date there have been few analytical or numerical studies on three-dimensional crack configurations. In particular, we note the work of Itou (1980) who used eigenfunction expansions and integral transforms to formulate solutions for a rectangular crack with a normally incident plane wave. The same method was employed by Krenk and Schmidt (1982) for a circular crack under oblique incidence. Lin and Keer (1987), Budreck and Achenbach (1988) and Nishimura and Kobayashi (1988) applied the boundary integral equation method (BIEM) to tackle scattering problems by cracks of arbitrary shapes.

The aim of this paper is to solve the direct problem of scattering of obliquely incident longitudinal plane waves from a prescribed rectangularly shaped crack. The motivation for this study stems from the possible existence of rectangularly shaped cracks in composite materials, caused for example, by pinning, and also from an interest in the role of the corner in influencing the scattered far-field. The latter effect cannot be found in the study of elliptical cracks or cracks with smoothly varying edges.

Similar to the approach employed by Itou (1980), eigenfunction expansions and integral transforms are used in Section 2 to formulate the governing equations for the present problem. Analytical results are derived in Section 3 for the scattered far-fields together with their Rayleigh limit. The criteria used to bound the computational errors are described in Section 4, followed by discussions of the numerical results for near-field crack opening displacements ($\mathscr{COD}$) and stress intensity factors ($\mathscr{SIF}$), and also for the far-field scattering patterns.

2. FORMULATION OF THE SCATTERING PROBLEM

2.1. *Mathematical preliminaries*

The response of an isotropic elastic solid is expressed as the superposition of the complex valued incident and scattered displacement fields

$$u_i^{\text{tot}}(\mathbf{x}) = u_i^{\text{in}}(\mathbf{x}) + u_i^{\text{sc}}(\mathbf{x}), \tag{1}$$

where the superscript "tot" denotes the total field, "in" the incident field and "sc" means the scattered field caused by the incidence. Latin subscripts run from 1 to 3, and the summation convention is implied throughout for the repetition of indices unless otherwise stated. Also, the subscript "0" will be used to denote quantities associated with the incident wave. The assumption in these equations and what follows is a time dependence of $e^{-i\omega t}$ in all fields, where $\omega > 0$ is the circular frequency. This dependence is to be understood and will be suppressed.

For an arbitrarily oriented incident plane wave,

$$u_i^{\text{in}}(x) = \mathscr{A}_u^{\text{in}}\, d_i\, e^{ik_0 p_j x_j}, \tag{2}$$

where $\mathscr{A}_u^{\text{in}}$ is the amplitude, the unit vectors $\mathbf{p}$ and $\mathbf{d}$ define directions of propagation and polarization respectively, and $k_0 = k_{\text{L}}$ or k_{T} is the incident wave number,

$$k_{\text{L}} = \frac{\omega}{C_{\text{L}}}, \quad k_{\text{T}} = \frac{\omega}{C_{\text{T}}}; \quad C_{\text{L}} = \sqrt{\frac{\lambda+2\mu}{\rho}}, \quad C_{\text{T}} = \sqrt{\frac{\mu}{\rho}}; \tag{3}$$

where ρ is the mass density, λ, μ are the Lamé constants, and C_{L} and C_{T} are the longitudinal and transverse wave speeds for the material.

The scattered displacement fields are constructed as an integral representation by employing the second Green's identity at an observation point x away from the crack. Thus

$$u_l^{\text{sc}}(\mathbf{x}) = \int_{\mathscr{S}} u_i^{\text{sc}}(\mathbf{x}')\Sigma_{ij;l}(\mathbf{x}'-\mathbf{x})n_j(\mathbf{x}')\, d\mathscr{S}(\mathbf{x}'), \tag{4}$$

with the source point $\mathbf{x}'$ running over the entire crack surfaces $\mathscr{S} = \mathscr{C}^+ \cup \mathscr{C}^-$, where $\mathscr{C}^+$ and $\mathscr{C}^-$ are the surfaces facing down and up respectively. Also, $\Sigma_{ij;l}(\mathbf{x}'-\mathbf{x})$ denote the elasto–dynamic stress fields at an observation point $\mathbf{x}$ caused by the application of a unit force at a source point $\mathbf{x}'$ in the lth direction, and $n_j^{\pm} = \pm\delta_{3j}$ denotes the surface unit normal, see Fig. 1. The crack opening displacement field ($\mathscr{COD}$) is defined in the crack

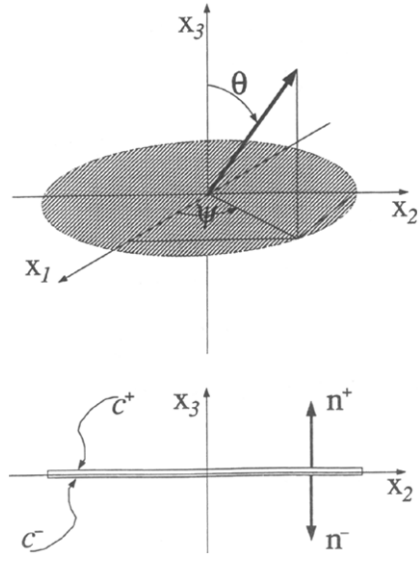

Fig. 1. The coordinate systems.

plane by

$$u_i^{\text{tot}}(x_1, x_2, 0^+) - u_i^{\text{tot}}(x_1, x_2, 0^-) = u_i^{\text{sc}}(x_1, x_2, 0^+) - u_i^{\text{sc}}(x_1, x_2, 0^-)$$
$$= \begin{cases} 0, & x_1, x_2 \text{ off crack}; \\ \Delta u_i^{\text{sc}}(x_1, x_2), & x_1, x_2 \text{ on crack}. \end{cases} \tag{5}$$

Using $n_3^+ = -n_3^-$ and (5), eqn (4) eventually simplifies to a surface integral over the upper face of the crack only

$$u_l^{\text{sc}}(x) = \int\int_{\mathscr{C}^+} \mathrm{d}x_1' \, \mathrm{d}x_2' \, \Delta u_i^{\text{sc}}(\mathbf{x}') \Sigma_{i3;jl}(\mathbf{x}' - \mathbf{x}). \tag{6}$$

2.2. *Derivation of the integral equations*

Application of standard procedures (Achenbach *et al.*, 1982) leads to the following integral form of the Green's function for an isotropic elastic solid with $x_3 \geqslant x_3'$,

$$\Sigma_{ij;jl}(\mathbf{x}' - \mathbf{x}) = \frac{1}{8\pi^2} \int\int_{-\infty}^{\infty} \mathrm{d}k_1 \, \mathrm{d}k_2 \left\{ \frac{1}{v_{\text{L}}} k_l^{\text{L}} \left[\left(1 - 2\frac{C_{\text{T}}^2}{C_{\text{L}}^2} \right) \delta_{ij} + \frac{2}{k_{\text{T}}^2} k_i^{\text{L}} k_j^{\text{L}} \right] \mathrm{e}^{ik_j^{\text{L}}(x_j' - x_j)} \right.$$
$$\left. + \frac{1}{v_{\text{T}}} \left[k_i^{\text{T}} \delta_{jl} + k_j^{\text{T}} \delta_{il} - \frac{2}{k_{\text{T}}^2} k_i^{\text{T}} k_j^{\text{T}} k_l^{\text{T}} \right] \mathrm{e}^{ik_j^{\text{T}}(x_j' - x_j)} \right\}, \tag{7}$$

and when substituted into (6) gives the following formula for the scattered displacement for all values of x_3:

$$u_l^{\text{sc}}(x) = \int\int_{\mathscr{C}^+} \mathrm{d}x_1' \, \mathrm{d}x_2' \, \Delta u_i^{\text{sc}}(x_1', x_2') \frac{1}{8\pi^2} \int\int_{-\infty}^{\infty} \mathrm{d}k_1 \, \mathrm{d}k_2 \, \mathrm{e}^{i[k_1(x_1 - x_1') + k_2(x_2 - x_2')]} \mathscr{B}_u^{il}(k_1, k_2; x_3). \tag{8}$$

In these expressions

$$\mathscr{B}_u^{il}(k_1, k_2; x_3) = \frac{1}{v_{\text{L}}} k_l^{\text{L}} \left[\left(1 - 2\frac{C_{\text{T}}^2}{C_{\text{L}}^2} \right) \delta_{i3} + \frac{2}{k_{\text{T}}^2} k_i^{\text{L}} v_{\text{L}} \right] \mathrm{e}^{\mathrm{i}v_{\text{L}}|x_3|}$$
$$+ \frac{1}{v_{\text{T}}} \left[k_i^{\text{T}} \delta_{3l} + v_{\text{T}} \delta_{il} - \frac{2}{k_{\text{T}}^2} k_i^{\text{T}} v_{\text{T}} k_l^{\text{T}} \right] \mathrm{e}^{\mathrm{i}v_{\text{T}}|x_3|}, \tag{9}$$

where the wave number vectors $\mathbf{k}^\gamma$ are

$$\mathbf{k}^\gamma = \{k_1, k_2, v_\gamma\}, \quad (\gamma = \text{L}, \text{T}). \tag{10}$$

The equations of motion and the radiation condition at infinity imply that $\text{Im}\,(v_\gamma) \geqslant 0$, and

$$v_\gamma = \begin{cases} \sqrt{k_\gamma^2 - k_1^2 - k_2^2}, & \text{for } k_\gamma^2 > k_1^2 + k_2^2; \\ \mathrm{i}\sqrt{k_1^2 + k_2^2 - k_\gamma^2}, & \text{for } k_\gamma^2 < k_1^2 + k_2^2; \end{cases} \quad (\gamma = \text{L}, \text{T}). \tag{11}$$

Following the derivation of (8), the corresponding scattered stress fields are

$$\sigma_{i3}^{\text{sc}}(x) = \frac{\mathrm{i}}{8\pi^2} \int\int_{-\infty}^{\infty} \mathrm{d}k_1 \, \mathrm{d}k_2 \, \mathrm{e}^{\mathrm{i}(k_1 x_1 + k_2 x_2)} \mathscr{B}_\sigma^{i3l}(k_1, k_2; x_3)$$
$$\times \int\int_{\mathscr{C}^+} \mathrm{d}x_1' \, \mathrm{d}x_2' \, \mathrm{e}^{-\mathrm{i}(k_1 x_1' + k_2 x_2')} \Delta u_l^{\text{sc}}(x_1', x_2'), \tag{12}$$

where

$$\mathscr{B}_\sigma^{ijl} = \frac{1}{v_L}(\lambda k_L^2 \delta_{ij} + 2\mu k_j^L)\left[\left(1 - 2\frac{C_T^2}{C_L^2}\right)\delta_{l3} + \frac{2}{k_T^2} k_l^L v_L\right] e^{iv_L|x_3|}$$

$$+ \frac{1}{v_T}\mu\left[(k_i^T \delta_{3j} + k_j^T \delta_{3i})k_l^T + (k_i^T \delta_{lj} + k_j^T \delta_{li})v_T - \frac{4}{k_T^2} k_i^T k_j^T k_l^T v_T\right] e^{iv_T|x_3|}. \quad (13)$$

The term $\mathscr{B}_\sigma^{i3l}$ physically represents the effect of the $\mathscr{COD}$ component in the lth direction on a stress component along the ith direction in the crack plane oriented in the x_3 dimension. We note the symmetry property $\mathscr{B}_\sigma^{i3l} = \mathscr{B}_\sigma^{l3i}$. Also, it is instructive to write out $\mathscr{B}_\sigma^{i3l}(k_1, k_2; 0)$ explicitly so that one may readily see the decoupling of the in-plane and out-of-plane terms with respect to the crack plane $x_3 = 0$:

$$\frac{\mathscr{B}_\sigma^{i3l}}{\mu} = \begin{bmatrix} k_1^2\left[\frac{4}{k_T^2}(v_L - v_T) + \frac{1}{v_T}\right] + v_T, & k_1 k_2\left[\frac{4}{k_T^2}(v_L - v_T) + \frac{1}{v_T}\right], & 0 \\ k_1 k_2\left[\frac{4}{k_T^2}(v_L - v_T) + \frac{1}{v_T}\right], & k_2^2\left[\frac{4}{k_T^2}(v_L - v_T) + \frac{1}{v_T}\right] + v_T, & 0 \\ 0 & 0 & \frac{k_T^2}{v_L}\left[1 - \frac{2}{k_T^2}(k_1^2 + k_2^2)\right]^2 + \frac{4}{k_T^2} v_T (k_1^2 + k_2^2) \end{bmatrix}. \quad (14)$$

Great advantages will emerge from this decoupling property in some of the subproblems dealt with in Section 4.

The traction-free boundary condition on the crack surface implies

$$\sigma_{i3}^{in} + \sigma_{i3}^{sc} = 0, \quad \text{where } x_3 = 0. \quad (15)$$

Equations (2), (12) and (15) imply that, for all x_1, x_2 on the crack plane,

$$0 = 8\pi^2 \mathscr{A}_u^{in} k_0 [\lambda \, d_k p_k \delta_{i3} + \mu(d_i p_3 + d_3 p_i)] \, e^{ik_0(p_1 x_1 + p_2 x_2)}$$

$$+ \int\int_{-\infty}^{\infty} dk_1 \, dk_2 \, e^{i(k_1 x_1 + k_2 x_2)} \mathscr{B}_\sigma^{i3l} \int\int_{\mathscr{C}^+} dx_1' \, dx_2' \, e^{-i(k_1 x_1' + k_2 x_2')} \Delta u_l^{sc}(x_1', x_2'), \quad (16)$$

where the first term on the right-hand side stands for the incident stress fields, and the second bears the physical interpretation of the total scattered stress fields emitted from all the secondary sources distributed over the entire crack face $\mathscr{C}^+$. The identities (16) are the integral equations to be solved for the sought unknown $\mathscr{COD}$ fields Δu_l^{sc}. Note that there are three integral equations which must be satisfied simultaneously everywhere on the crack plane. By the nature of the elasto-dynamic stress field (14), the third equation ($i = 3$) stands on its own, while the other two are generally coupled together. The major difficulty of solving these integral equations rests with the Green's function, which in the present formulation is expressed as a double integral of infinite extent.

3. SOLUTION OF THE INTEGRAL EQUATIONS

3.1. *Reduction to a system of linear equations*

We proceed to solve the integral equations by expanding the $\mathscr{COD}$ in terms of a complete set of functions, each of which tends to zero at the edges of the crack in a square

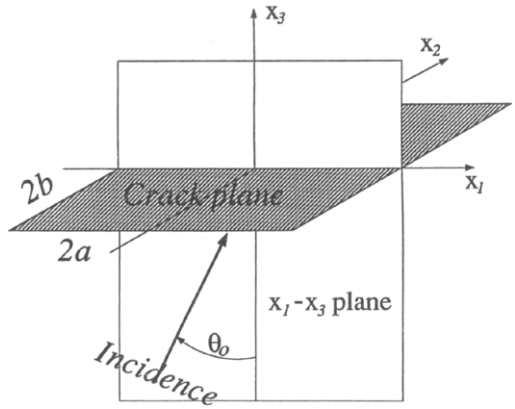

Fig. 2. The rectangular crack.

root sense. For the rectangular crack, $|x_1| \leqslant a$ and $|x_2| \leqslant b$, see Fig. 2, a suitable set of functions is the following

$$\phi_l(\zeta) = \begin{cases} \dfrac{1}{l}\cos\left[l \sin^{-1}(\zeta)\right], & (\text{odd } l); \\ \dfrac{i}{l}\sin\left[l \sin^{-1}(\zeta)\right], & (\text{even } l). \end{cases} \tag{17}$$

These are related to Chebyshev functions of the first kind. The $\mathscr{COD}$ is then assumed to be

$$\Delta u_i^{\mathrm{sc}}(x_1', x_2') = \mathscr{A}_u^{\mathrm{in}} \sum_{m=1}^{\infty} \sum_{n=1}^{\infty} \alpha_{mn}^{l} \phi_m\left(\frac{x_1'}{a}\right) \phi_n\left(\frac{x_2'}{b}\right). \tag{18}$$

Substituting (18) into (16) and using the identity

$$\int_{-1}^{1} \mathrm{d}\zeta\, \phi_l(\zeta)\, \mathrm{e}^{-ik\zeta} = \frac{\pi}{k} J_l(k), \tag{19}$$

where J_l is the lth order Bessel function, yields an infinite linear system of equations

$$\sum_{m=1}^{\infty} \sum_{n=1}^{\infty} \alpha_{mn}^{l} \bar{\mathscr{Q}}_{mnpq}^{li} = \bar{\mathscr{A}}_{pq}^{i}, \quad (p, q = 1, 2, \ldots), \tag{20}$$

where

$$\bar{\mathscr{Q}}_{mnpq}^{li} = \int_{-\infty}^{\infty} \mathrm{d}\xi \frac{J_m(\xi)}{\xi} \frac{J_p(\xi)}{\xi} \int_{-\infty}^{\infty} \mathrm{d}\eta \frac{J_n(\tau\eta)}{\tau\eta} \frac{J_q(\tau\eta)}{\tau\eta} \bar{\mathscr{B}}_{\sigma}^{i3l}(\xi, \eta), \tag{21}$$

$$\bar{\mathscr{A}}_{pq}^{i} = -\frac{8}{\tau} 2\bar{k}_{\mathrm{L}} \left[\left(\frac{\nu}{1-2\nu}\right)\delta_{i3} + \mathrm{d}_i^{\mathrm{L}}\, \mathrm{d}_3^{\mathrm{L}}\right] \frac{J_p(\xi_0)}{\xi_0} \frac{J_q(\tau\eta_0)}{\tau\eta_0}, \tag{22}$$

and ν is Poisson's ratio of the material. The over-bar in these expressions and what follows denotes the normalized version of quantities, and the dimensionless variables are defined as $\xi = ak_1$, $\eta = ak_2$, $\bar{k}_{\mathrm{L}} = ak_{\mathrm{L}}$, $\bar{k}_{\mathrm{T}} = ak_{\mathrm{T}}$, $\bar{v}_{\mathrm{L}} = av_{\mathrm{L}}$, $\bar{v}_{\mathrm{T}} = av_{\mathrm{T}}$. The parameter $\tau = b/a$ is the constant aspect ratio, and a superscript "L" is employed for the polarization vector **d** since only longitudinal incident waves are considered in this paper. It is significant to note that each element in the matrix of the governing equations (20) is a double integral of infinite

extent, the kernel of which possesses no singularity. This is a superior feature of the present method over the boundary integral equation method (BIEM) which is extensively used in solving scattering problems for cracks. Also, the decoupling property noted previously is evident by rewriting (20) in the explicit form

$$\sum_{m=1}^{\infty}\sum_{n=1}^{\infty}[\alpha_{mn}^{1}\bar{\mathcal{D}}_{mnpq}^{11}+\alpha_{mn}^{2}\bar{\mathcal{D}}_{mnpq}^{21}]=\bar{\mathcal{A}}_{pq}^{1}, \tag{23}$$

$$\sum_{m=1}^{\infty}\sum_{n=1}^{\infty}[\alpha_{mn}^{1}\bar{\mathcal{D}}_{mnpq}^{12}+\alpha_{mn}^{2}\bar{\mathcal{D}}_{mnpq}^{22}]=\bar{\mathcal{A}}_{pq}^{2}, \tag{24}$$

$$\sum_{m=1}^{\infty}\sum_{n=1}^{\infty}[\alpha_{mn}^{3}\bar{\mathcal{D}}_{mnpq}^{33}]=\bar{\mathcal{A}}_{pq}^{3}. \tag{25}$$

3.2. *Far-field asymptotics*

Some general features of the far-field scattering can be deduced without explicitly solving the system (20). In the far-field, $R=|x|\to\infty$, the scattered displacement becomes

$$u_i^{sc\infty}\sim-\left(\frac{i\pi}{4}\tau a^2\right)\mathcal{A}_u^{in}k_L\left[\mathcal{A}_i^{L}g^{L}+\left(\frac{k_T}{k_L}\right)\mathcal{A}_i^{T}g^{T}\right]. \tag{26}$$

The far-field scattering amplitudes are defined by

$$\mathcal{A}_i^{L}=n_i\sum_{m=1}^{\infty}\sum_{n=1}^{\infty}\alpha_{mn}^{l}\mathcal{F}_l^{L}, \tag{27}$$

$$\mathcal{A}_i^{T}=\sum_{m=1}^{\infty}\sum_{n=1}^{\infty}\alpha_{mn}^{l}\mathcal{F}_{il}^{T}, \tag{28}$$

the direction functions are

$$\mathcal{F}_l^{L}(\mathbf{n})=\left[\left(1-2\frac{C_T^2}{C_L^2}\right)\delta_{l3}+2\frac{C_T^2}{C_L^2}n_ln_3\right]\frac{J_m(k_La n_1)}{k_La n_1}\frac{J_n(k_Lb n_2)}{k_Lb n_2}, \tag{29}$$

$$\mathcal{F}_{il}^{T}(n)=(n_l\delta_{i3}+n_3\delta_{il}-2n_in_ln_3)\frac{J_m(k_Ta n_1)}{k_Ta n_1}\frac{J_n(k_Tb n_2)}{k_Tb n_2}, \tag{30}$$

where $\mathbf{n}=\mathbf{x}/R$ is the observation direction, and the scattered longitudinal and transverse spherical waves are

$$g^{L}(R)=\frac{e^{ik_LR}}{R},\quad g^{T}(R)=\frac{e^{ik_TR}}{R}. \tag{31}$$

Expression (26) shows that at field points which are remote from the crack the scattered fields decompose into longitudinal and transverse components polarized perpendicular to each other, namely $\mathcal{A}_i^{L}\mathcal{A}_i^{T}=0$. Also, the dependence of these far-fields on the distance from the centroid of the crack (31) is completely separated from their directional variations (27, 28), and only the latter parts contain the scattering information.

It is informative to explore the Rayleigh or long-wavelength limit of the scattered far-fields. Gubernatis and Domany (1979) expressed the far-field scattered displacement for an arbitrarily shaped cavity as

$$u_i^{sc\infty}\sim\mathcal{A}_i^{L}g^{L}+\mathcal{A}_i^{T}g^{T}, \tag{32}$$

and used the orthogonality property between the two scattered far-fields to define a vector **f** such that

$$\mathscr{A}_i^{\mathrm{L}} = n_i n_j f_j), \quad \mathscr{A}_i^{\mathrm{T}} = (\delta_{ij} - n_i n_j) f_j, \tag{33}$$

where **f** is written in terms of volume integrals. The static Eshelby solutions for ellipsoidal inclusions were then employed by Gubernatis and Domany to obtain the quasi-static approximation of **f** which turned out to have a leading order of ω^2. By letting the volume of the cavity tend to zero several characteristics of the scattered far-fields were recognized for crack identification and hence called the crack scattering signatures. For the present rectangular crack, it follows from (27) and (28) that when $k_{\mathrm{L}} a \ll 1$, the vector **f** becomes simply

$$f_j = \frac{\alpha_{11}^l}{4}\left[\left(1-2\frac{C_{\mathrm{T}}^2}{C_{\mathrm{L}}^2}\right)\delta_{l3} n_j - 2\left(1-\frac{C_{\mathrm{T}}^2}{C_{\mathrm{L}}^2}\right) n_j n_l n_3 + n_l \delta_{j3} + n_3 \delta_{jl}\right]. \tag{34}$$

It is clear in (33) and (34) that reversal of the observation direction, $\mathbf{n} \to -\mathbf{n}$, has no impact on the amplitudes of the far-field spherical waves. This means, as was explained by Gubernatis and Domany (1979), that the waves will be seen identically from two diametrically opposite directions (**n** and $-\mathbf{n}$); and, more importantly, this is the unique feature which distinguishes an arbitrary-shaped crack from volumetric defects. Also, if the incident longitudinal plane wave is directed either perpendicular ($\theta_0 = 0°$) or parallel ($\theta_0 = 90°$) to the crack plane, see Fig. 2, only the terms involving α_{11}^3 in (34) remain, implying

$$\mathscr{A}^{\mathrm{L}} \to \frac{|\alpha_{11}^3|}{4}\frac{\nu}{1-\nu}\left(1+\frac{1-2\nu}{\nu}\cos^2\theta\right), \tag{35}$$

$$\mathscr{A}^{\mathrm{T}} \to \frac{|\alpha_{11}^3|}{4}|\sin 2\theta|. \tag{36}$$

Note that these results have no dependence on the polar angle ψ, and are symmetric about the crack plane ($\theta = 90°$). In summary, as stated by Gubernatis and Domany (1979), these long-wavelength scattering signatures can be utilized to determine the orientation of a flat crack.

For the perfectly elastic material considered in this project no energy dissipation is expected. Hence, the time average of the total energy flux must vanish within any surface $\mathscr{S}$ enclosing the entire crack, implying (Achenbach, 1982)

$$\frac{\omega}{2}\mathrm{Im}\int\!\!\int_{\mathscr{S}} (\mathbf{tu}^*)\, \mathrm{d}\mathscr{S} = 0, \tag{37}$$

where **t** is the traction on $\mathscr{S}$ and * denotes complex conjugate. By allowing the surface $\mathscr{S}$ to tend to infinity and using the method of stationary phase, we obtain the scattered-power theorem

$$\int_0^{\pi} \sin\theta\, \mathrm{d}\theta \int_0^{2\pi} \mathrm{d}\psi \left[|\mathscr{A}^{\mathrm{L}}|^2 + \left(\frac{k_{\mathrm{T}}}{k_{\mathrm{L}}}\right)|\mathscr{A}^{\mathrm{T}}|^2\right] + \left(\frac{16}{\tau k_{\mathrm{L}}^2 a^2}\right)\mathrm{Re}\,[\mathscr{A}^{\mathrm{L}}(\mathbf{d}^{\mathrm{L}})] = 0, \tag{38}$$

where

$$\mathrm{Re}\,[\mathscr{A}^{\mathrm{L}}(\mathbf{d}^{\mathrm{L}})] = \sum_{m=1}^{\infty}\sum_{n=1}^{\infty} \mathrm{Re}\,[\alpha_{mn}^l]\mathscr{F}_l^{\mathrm{L}}(\mathbf{d}^{\mathrm{L}}). \tag{39}$$

The first term in (38) represents the total scattered flux, and the second bears the physical significance of the interference between the incident wave and the scattered fields along the forward direction of the incidence $\mathbf{d}^{\mathrm{L}}$. The fact that only $\mathscr{F}_l^{\mathrm{L}}$ is present in the interference term originates from the longitudinal nature of the incidence and the orthogonality relation

$\mathscr{A}_i^{\mathrm{L}}\mathscr{A}_i^{\mathrm{T}} = 0$. The total scattering cross-section is defined as the time average of the ratio between the total scattered energy and the incident flux over a unit area. Thus,

$$\Sigma(\omega) = \frac{\langle \mathscr{P}^{\mathrm{sc}} \rangle_{\mathscr{S}}}{\langle \mathscr{P}^{\mathrm{in}} \rangle} = \left[\frac{\omega}{2}\,\mathrm{Im}\int\!\!\int_{\mathscr{S}} t_i^{\mathrm{sc}} u_i^{\mathrm{sc}*}\,\mathrm{d}\mathscr{S}\right] \Big/ \left[\frac{\omega}{2}\,\mathrm{Im}\,(\sigma_{ij}^{\mathrm{in}}\,\mathrm{d}_j^{\mathrm{L}}\,u_i^{\mathrm{in}*})\right]$$

$$= -\frac{\pi^2}{4}(4\tau a^2)\,\mathrm{Re}\,[\mathscr{A}^{\mathrm{L}}(\mathbf{d}^{\mathrm{L}})], \tag{40}$$

where the final equality follows from (38).

4. NUMERICAL CALCULATIONS AND DISCUSSION

The bulk of the numerical calculations involves the evaluation of the double infinite integrals $\mathscr{Q}_{mnpq}^{li}$ in eqn (21). The integrands are even functions of their arguments and therefore the integrals only need to be computed in the first quadrant of the η–ξ plane. They are further split into four integrals for numerical computation

$$\mathscr{Q}_{mnpq}^{li} = 4\left[\int_0^{\alpha}\mathrm{d}\eta\int_0^{\alpha}\mathrm{d}\xi\,\mathscr{G}(\eta,\xi) + \int_0^{\alpha}\mathrm{d}\eta\int_{\alpha}^{\infty}\mathrm{d}\xi\,\mathscr{G}(\eta,\xi)\right.$$

$$\left. + \int_{\alpha}^{\infty}\mathrm{d}\eta\int_0^{\alpha}\mathrm{d}\xi\,\mathscr{G}(\eta,\xi) + \int_{\alpha}^{\infty}\mathrm{d}\eta\int_{\alpha}^{\infty}\mathrm{d}\xi\,\mathscr{G}(\eta,\xi)\right], \tag{41}$$

where $\mathscr{G}(\eta,\xi)$ is the integral kernel. Asymptotic approximations to the semi-infinite integrals are derived for a chosen large number $\alpha \gg 1$ through repeated integrations by parts and the use of the leading term in the asymptotic expressions of Bessel functions for large arguments. The finite integrals are computed by a composite Simpson's rule. The use of a pre-calculated data table for the Bessel functions actually reduced the computer CPU time by about an order of magnitude. The solution of a truncated version of the simultaneous equations (20) for the unknown expansion coefficients was accomplished via an algorithm based on Gaussian elimination with LU factorization. Evaluation of the other physical quantities which are represented explicitly by the expansion coefficients is then straightforward. To keep the numerical calculations reasonably simple the incident waves were restricted to be parallel to the x_1–x_3 plane, see Fig. 2.

Two accuracy control criteria were employed in the numerical process: the optimal truncation rule was used in the asymptotic evaluation of the semi-infinite integrals in order to bound the truncation error to a minimum (Bender and Orszag, 1978). A simple truncation procedure was applied to determine the number of terms needed in the simultaneous system of equations. Some results from different trunctions are compared in Fig. 3 which shows

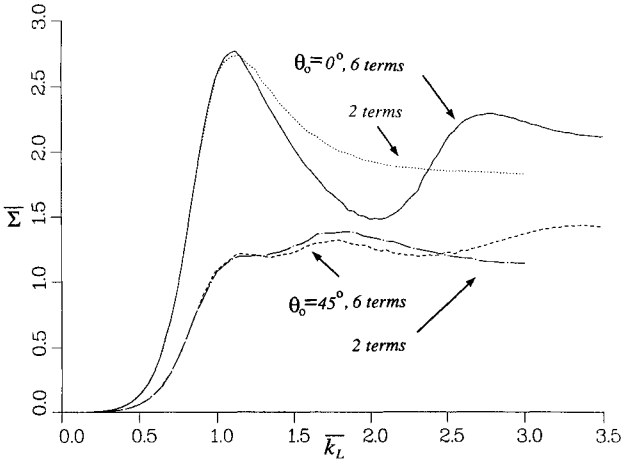

Fig. 3. A comparison to show the convergence of the expansions.

that with only two Chebyshev functions the $\mathscr{COD}$ can be fit very well in a low frequency regime where the dimensionless frequency $\bar{k}_L < 1$. Beyond that, six functions were found to be sufficient within the frequency range considered. The scattered-power theorem, eqn (38), served as a check on the over-all consistency of the numerical results. Thus, for all the numerical results discussed here, the two terms of this equation had a relative error of less than one percent. It should be noted that the scattered power theorem can only verify the consistency of the numerical results, but not the accuracy, since the results from the two truncation versions mentioned above both had less than 1% relative error in the entire frequency region $0 \leqslant \bar{k}_L \leqslant 3.5$.

4.1. *Crack opening displacements*

Before discussing dynamic results, we note that in the limit $\omega \to 0$ the system (20) reduces to the corresponding set of equations for an arbitrarily applied static load. We have numerically solved the static equations for a normal load P_0 in the x_3 direction, and found that the maximum crack opening displacement of a square crack ($\tau = 1$) appears at its centroid and is

$$\Delta u_{3(\text{square})}^{\text{Static}}(0,0) \approx 1.40\left(\frac{1-\nu}{\mu}\right)aP_0, \tag{42}$$

which is about 10% larger than the corresponding value for an inscribed penny shaped crack

$$\Delta u_{3(\text{penny})}^{\text{Static}}(0,0) = \frac{4}{\pi}\left(\frac{1-\nu}{\mu}\right)aP_0,$$

(Bui, 1977). Note that the difference in area between these two cracks is more than 27%.

Some of the dynamic $\mathscr{COD}$ profiles for a square crack are plotted in Figs 4–6. These $\mathscr{COD}$s have been normalized with respect to the right member of (42) with $P_0 = i\mathscr{A}_u^{\text{in}}k_0(\lambda+2\mu)$ for the dynamic load. For a normally incident wave of moderate frequency, the only non-zero component Δu_3^{sc} has the form shown in Fig. 4. This is clearly symmetric relative to both the x_1 and x_2 axes, which is also the case in the static limit. Under oblique incidence another component, Δu_1^{sc}, becomes non-zero, although one still has $\Delta u_2^{\text{sc}} = 0$ because the incident wave is assumed to be parallel to the x_1–x_3 plane. The

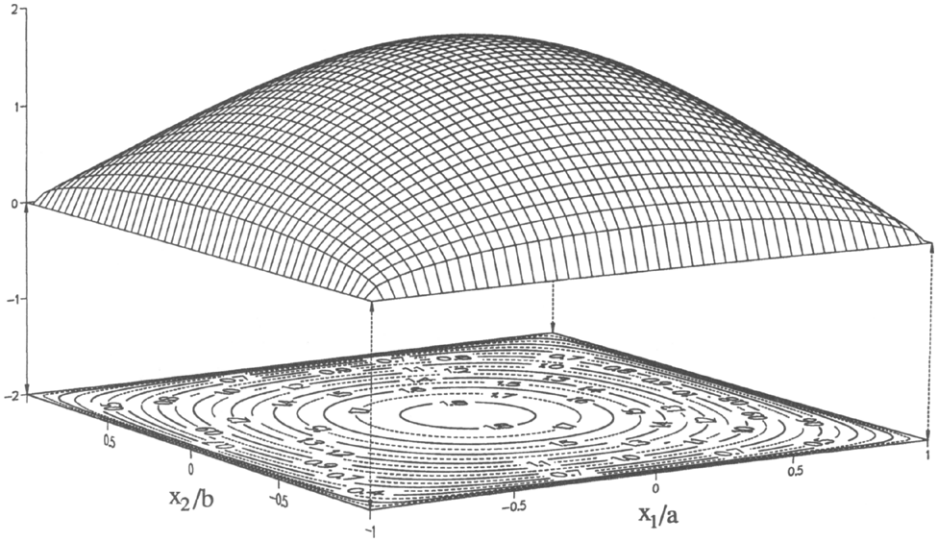

Fig. 4. $|\overline{\Delta u_3^{\text{sc}}}|$ for normally incident waves, $\bar{k}_L = 1$.

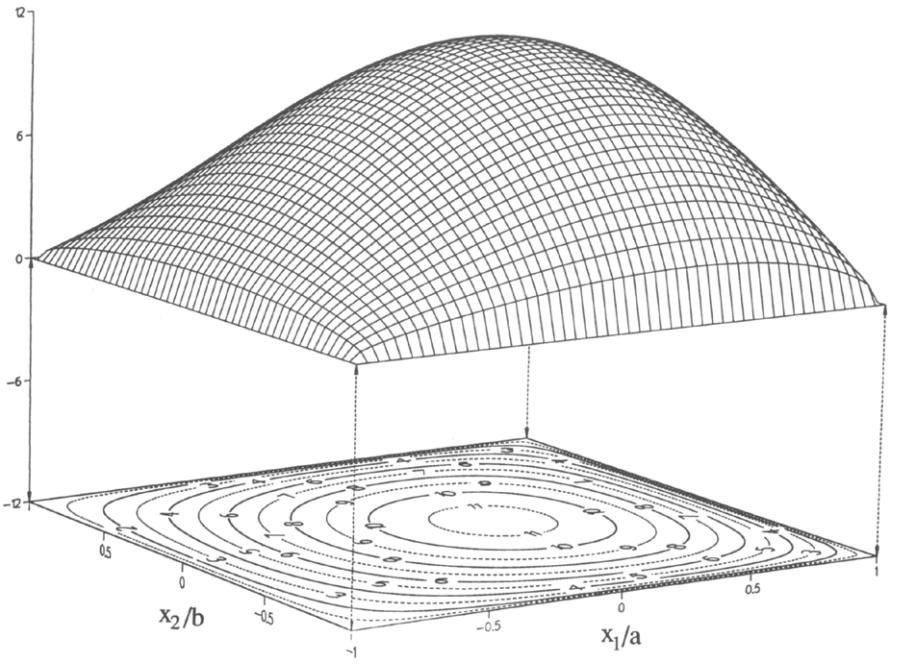

Fig. 5. $|\overline{\Delta u_3^{sc}}|$ for an obliquely incident wave with $\theta_0 = \pi/4$ at $\overline{k_L} = 1$.

dependence of the $\mathscr{COD}$ profiles on the incident angle is illustrated in Figs 5 and 6, and we note the changing shapes when the excitation frequency is high.

4.2. *Stress intensity factors*

Three possible types of stress intensity factor ($\mathscr{SIF}$) are defined as

$$K_I = \lim_{x_j' \to d} \left[\frac{\mu}{4(1-\nu)} \sqrt{\frac{2\pi}{d}} \frac{\Delta u_3(x_1', x_2')}{\sqrt{1-\bar{x}'}} \right] \quad j = \begin{cases} 1, & d = a, \\ 2, & d = b, \end{cases} \tag{43}$$

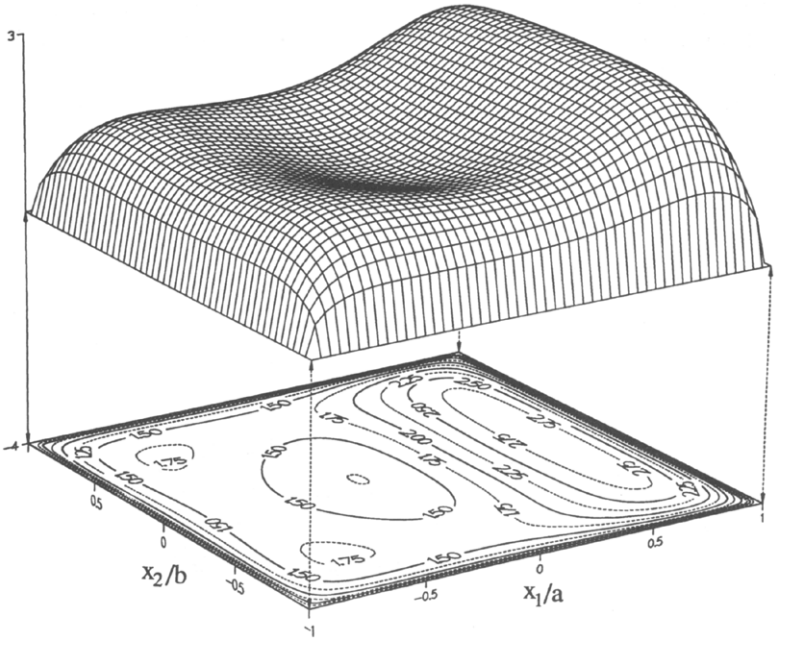

Fig. 6. $|\overline{\Delta u_1^{sc}}|$ for an obliquely incident wave with $\theta_0 = \pi/4$ at $\overline{k_L} = \pi$.

$$K_{\mathrm{II}\ell} = \lim_{x_1' \to a} \left[\frac{\mu}{4(1-\nu)} \sqrt{\frac{2\pi}{a}} \frac{\Delta u_1^{\mathrm{sc}}(x_1', x_2')}{\sqrt{1-\bar{x}'}} \right], \tag{44}$$

$$K_{\mathrm{IIIs}} = \lim_{x_2' \to b} \left[\frac{\mu}{4} \sqrt{\frac{2\pi}{\tau a}} \frac{\Delta u_1^{\mathrm{sc}}(x_1', x_2')}{\sqrt{1-\bar{x}'}} \right], \tag{45}$$

where $\bar{x}' = x_j'/d$. The Mode II and Mode III $\mathscr{SIF}$s have relatively simple expressions in the present problem owing to the specific orientation of the incident wave in conjunction with the inherent symmetry of rectangular cracks. Only the Mode I $\mathscr{SIF}$ is present for normal incidence; otherwise, all three modes exist. In the static limit the Mode I $\mathscr{SIF}$ achieves local maxima at the mid-points of the long (l) and short (s) edges, and can be simplified to

$$\bar{K}_{\mathrm{I}\ell}^{(\mathrm{rectangle})} = \frac{1}{2} \sum_{m=1}^{\infty} \sum_{n=1}^{\infty} \bar{\alpha}_{mn}^{\mathrm{Static}} \frac{1}{n} (-1)^{\frac{m-1}{2}}, \tag{46}$$

$$\bar{K}_{\mathrm{I}s}^{(\mathrm{rectangle})} = \frac{1}{2\sqrt{\tau}} \sum_{m=1}^{\infty} \sum_{n=1}^{\infty} \bar{\alpha}_{mn}^{\mathrm{Static}} \frac{1}{m} (-1)^{\frac{n-1}{2}}. \tag{47}$$

These results were normalized by $K_{\mathrm{Imax}}^{(2-D)} = \sqrt{\pi a} P_0$, the $\mathscr{SIF}$ for a two-dimensional plane-strain Griffith crack of length $2a$. For a square crack ($\tau = 1$), as shown in Fig. 7, we have

$$K_{\mathrm{Imax}}^{(\mathrm{square})} \approx 0.738 K_{\mathrm{Imax}}^{(2-D)}. \tag{48}$$

This result agrees very well with the data reported by both Weaver (1977) and Mastrojannis *et al.* (1979).

For rectangular cracks with increasing aspect ratio $\tau > 1$, the static limit discussed above gives the absolute maximum $K_{\mathrm{I}\ell}$ at the mid-point of each long edge, Fig. 7, and the value there approaches the corresponding $\mathscr{SIF}$ for a plane-strain Griffith crack when τ is large enough [$\tau \geqslant 3$, see Weaver (1977)]. The local maximum $K_{\mathrm{I}s}$ on the short edges behaves differently, and according to eqn (47) it decreases as the reciprocal of $\sqrt{\tau}$, in agreement with the numerical results. This phenomenon can be understood by considering the close analogy between a prolonged rectangular crack and an elliptical crack. In the latter case an exact expression exists for the Mode I $\mathscr{SIF}$, and a comparison of the $\mathscr{SIF}$ for elliptical cracks with different values of τ shows that the local maxima behave very much like those of the rectangular crack as a function of τ. Plots of the $\mathscr{SIF}$ for elliptical cracks may be found in the book by Sih and Liebowitz (1968). By a modest stretch of the imagination we may ascribe these changes in the local $\mathscr{SIF}$ maxima to a St Venant

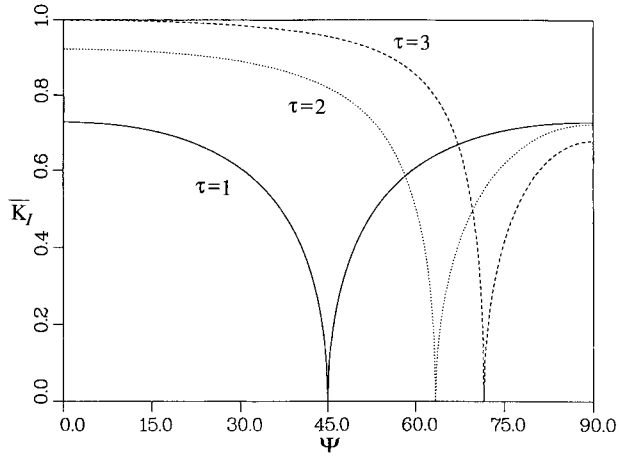

Fig. 7. $\bar{K}_{\mathrm{I}}^{(\mathrm{rectangle})}$ versus polar angles ψ for different aspect ratios.

phenomenon. Thus, for a rectangular crack which is gradually elongated, the constraint posed on the mid-portion of the long edges by the short ones attenuates, and the $\mathscr{SIF}$ in this portion tends to the value for a two-dimensional Griffith crack. By the same reasoning, as the long edges are extended, their influence on the short ones in turn becomes stronger, and this is related to the decrease of the local maxima of $\mathscr{SIF}$.

We note that different features were predicted along the short edges in the paper by Weaver (1977). However, a careful study reveals that Weaver's results were based on a different mathematical model of the rectangular crack than used here. In particular, the maximum value of the $\mathscr{SIF}$ was estimated using an energy method which allows only the short edges of the rectangular crack to grow while fixing the long edges (Budiansky, 1990). Thus, the predictions of Weaver are not in conflict with the present results.

In the finite frequency region $0 \leqslant \bar{k}_L \leqslant 3.5$, the maximum K_I for a square crack is displayed in Fig. 8. The first peak on the solid curve appears at about $\bar{k}_L = 0.85$, and its value is about 65% higher than the corresponding static limit. The second peak occurs around $\bar{k}_L = 2.6$, and has a magnitude of 0.84. These data match very well with the results reported by Nishimura and Koboyashi (1988). The first peak is slightly higher than the corresponding value given by Itou (1980) where the frequency range of his computations was $0 \leqslant \bar{k}_L \leqslant 1.5$.

Using a membrane analogy, after Budreck and Achenbach (1988), the "resonant" frequencies of the first two Rayleigh modes of the crack faces are found to be $\bar{k}_{LR_1} = 0.87$ and $\bar{k}_{LR_2} = 2.62$. These can explain the occurrence of the two peaks found on the K_I curve as the constructive interference between the incident wave and the excited standing Rayleigh surface modes on the traction-free crack faces. The membrane analogy is also helpful in understanding the origin of the peaks appearing on the maximum K_I curves for rectangular cracks under normal incidence, plotted in Fig. 9. When the aspect ratio $\tau > 1$, two distinct Rayleigh mode frequencies can be estimated for the x_1 and x_2 directions separately, and the resonant frequency for the true drum-head mode of the crack faces can be obtained as a simple combination of the two. This procedure gives $\bar{k}_{LR_1} = 0.655$ for $\tau = 2$ and $\bar{k}_{LR_1} = 0.582$ for $\tau = 3$, which correlate well with the positions of the primary peaks in Fig. 9. The relatively constant position of the secondary peaks can be explained by the dominant effect of the second Rayleigh mode along the short dimension of the cracks.

A general observation can be made concerning the order of appearance of the primary peaks in Fig. 9: the more a rectangular crack is prolonged, the lower the frequency at which the peak appears. This is consistent with the statement made by Budreck and Achenbach (1988) for elliptical cracks.

The Mode I $\mathscr{SIF}$s of three rectangular cracks under an oblique incidence, with $\theta_0 = 45°$, are shown in Fig. 10. The high secondary peaks occurring in Fig. 10 are understood to be caused by the second anti-symmetric Rayleigh modes which do not exist when the crack is under normal loading.

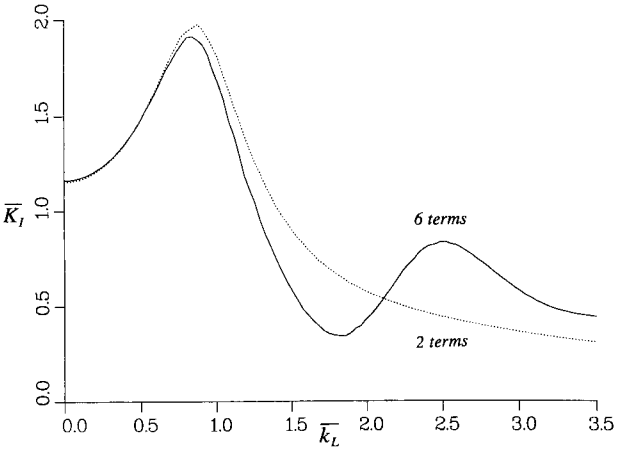

Fig. 8. $|\bar{K}_I^{(\text{square})}|$ versus normalized frequency k_L.

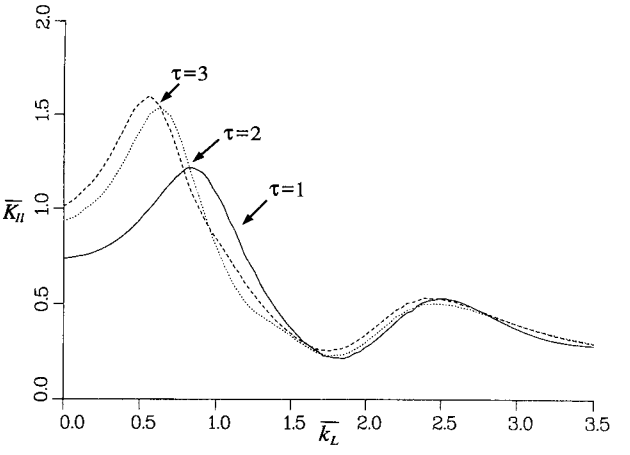

Fig. 9. $|\bar{K}_{II}^{(rectangle)}|$ versus frequency $\bar{k}_L$, for $\theta_0 = 0°$.

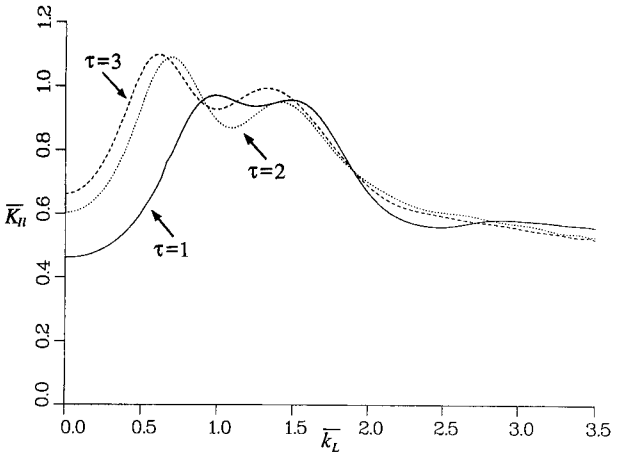

Fig. 10 $|\bar{K}_{II}^{(rectangle)}|$ versus frequency $\bar{k}_L$, for $\theta_0 = 45°$.

4.3. *Scattering cross-sections*

The scattering cross-section defined in (40) is normalized by the area of the crack, $A = 4\tau a^2$, and some numerical results are shown in Figs 11 and 12. The computed values of $\bar{\Sigma}$ for rectangular cracks with different aspect ratio τ are plotted in Fig. 11 as a function

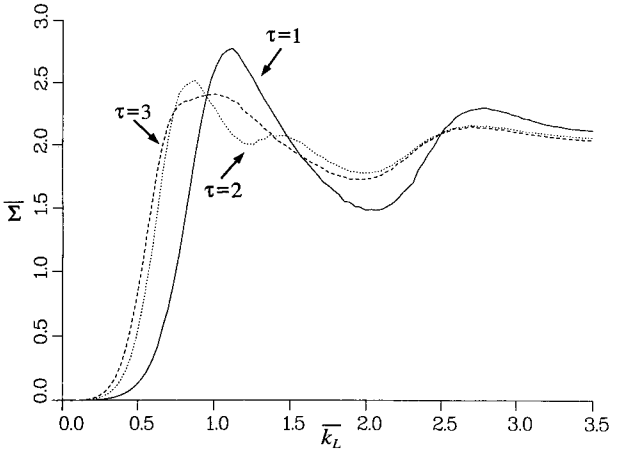

Fig. 11. $\bar{\Sigma}$ versus $\bar{k}_L$ for different aspect ratios τ and $\theta_0 = 0°$.

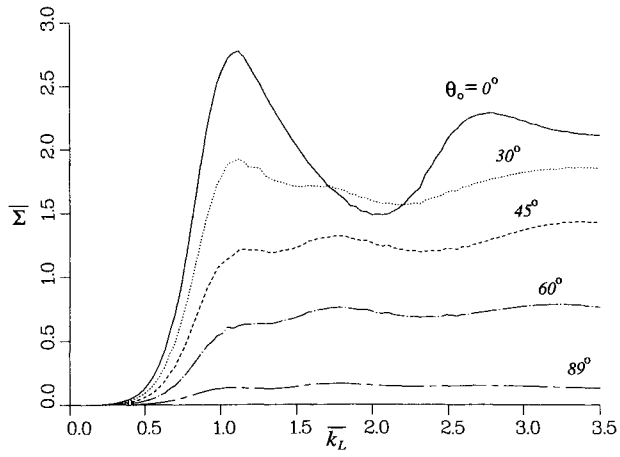

Fig. 12. $\bar{\Sigma}$ versus $\bar{k}_L$ for different incident angles θ_0 with $\tau = 1$.

of the dimensionless frequency. The high frequency asymptotes are virtually the same for normal incidence for the range of crack aspect ratios considered. The specific value, $\bar{\Sigma} \sim 2$, can be interpreted as both of the crack faces subtracting energy from the incident wave and converting it into scattered waves. The same value of 2 also follows from the use of the Kirchhoff approximation. It is not surprising that Budreck and Achenbach (1988) found exactly the same result for a circular crack, i.e. $\bar{\Sigma} \sim 2$, since in the high frequency regime the Kirchhoff approximation can be used for both rectangular and elliptical cracks. Note that the Kirchhoff approximation is independent of the boundary conditions at the crack edges.

The scattering cross-section is plotted in Fig. 12 for a square crack ($\tau = 1$) under different incident angles. The high frequency asymptotes of these curves display a simple relation to the incident angle which can be explained on the basis of physical elastodynamics or the Kirchhoff approximation. Thus, when the incident angles θ_0 are not very large, the scattered wave is dominated by the reflections, and the high frequency value of $\bar{\Sigma}$ can be estimated by the geometrical projection of the crack face onto the plane normal to the direction of incidence, which implies $\bar{\Sigma}(\theta_0) \sim 2 \cos \theta_0$. This estimation breaks down near grazing incidence, $\theta_0 = \pi/2$, because the crack edge diffraction dominates the scattered field in the frequency range considered.

4.4. *Scattering patterns*

The scattering patterns are defined by the scattering amplitudes of the far-field displacements, eqns (27) and (28). The physical significance of $\mathscr{A}_r^{\mathrm{L}}$ is the angular dependence of the far-field longitudinal wave, $\mathscr{A}_\theta^{\mathrm{T}}$ corresponds to the far-field SV-wave, while $\mathscr{A}_\psi^{\mathrm{T}}$ defines the angular dependence of the far-field SH-wave. These factors are illustrated in Figs 13–15 in the same way that Krenk and Schmidt (1982) used to represent the scattering patterns for a penny-shaped crack. In each of these figures the scattering pattern is characterized by a pair of graphs with a bird's-eye-view on the left looking down on the crack plane and side-views on the right for an observation direction in the crack plane (see also Figs 1 and 2). These patterns are symmetric to the x_1–x_3 plane, and therefore it is sufficient to show only half of them. Thus, in each bird's-eye-view the upper half depicts the pattern above the crack plane with heavy solid lines, and the lower half shows the contour lines of the pattern beneath the crack plane, and they are in lighter solid lines. In the side-views, solid or heavy chain-dot lines show the views looking in the positive x_2 (or Y) direction, and light dash lines represent the view in the negative x_1 (or X) direction in cases where this is different than the former view.

The scattering patterns for a square crack under normal incidence are shown in Figs 13 and 14. Comparisons of these with the counterparts published by Krenk and Schmidt (1982) for a circular crack show there is virtually no difference when the incident frequency

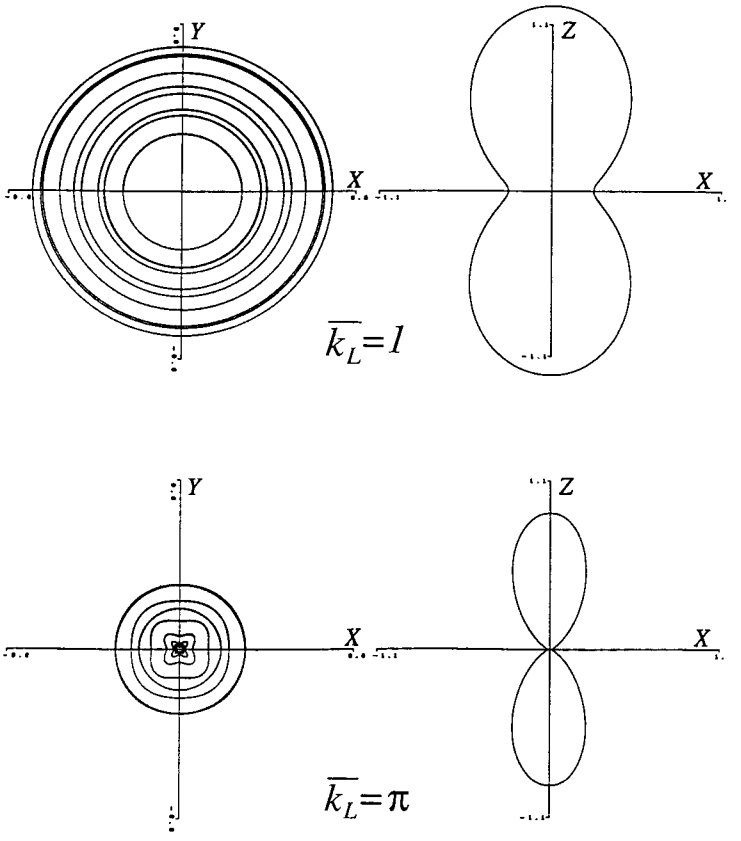

Fig. 13. Scattering patterns of $u_r^{sc,\gamma}$ due to normal incidence, $\theta_0 = 0$, $\tau = 1$.

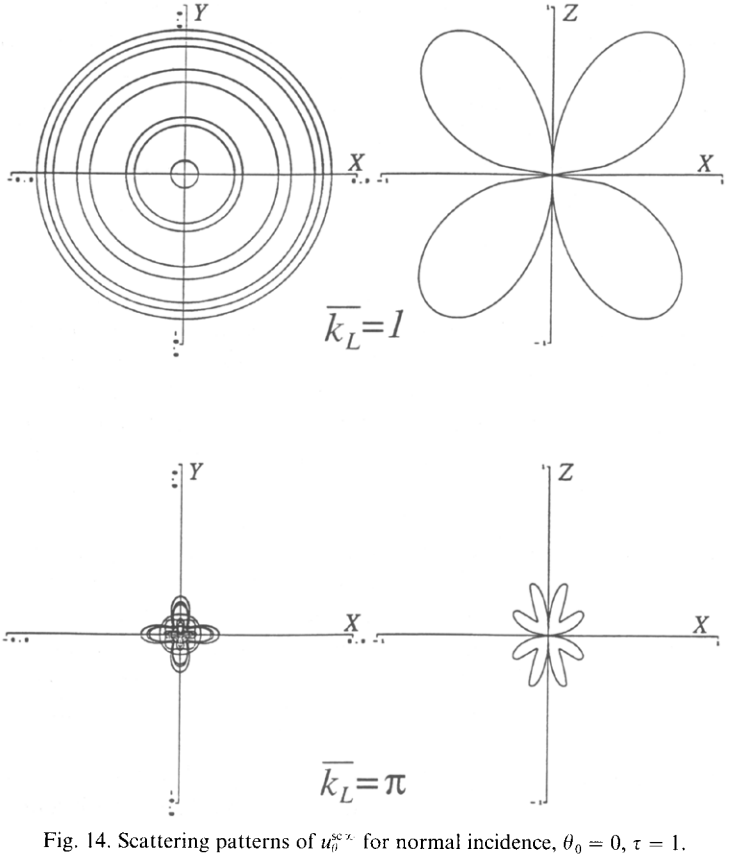

Fig. 14. Scattering patterns of $u_\theta^{sc,\gamma}$ for normal incidence, $\theta_0 = 0$, $\tau = 1$.

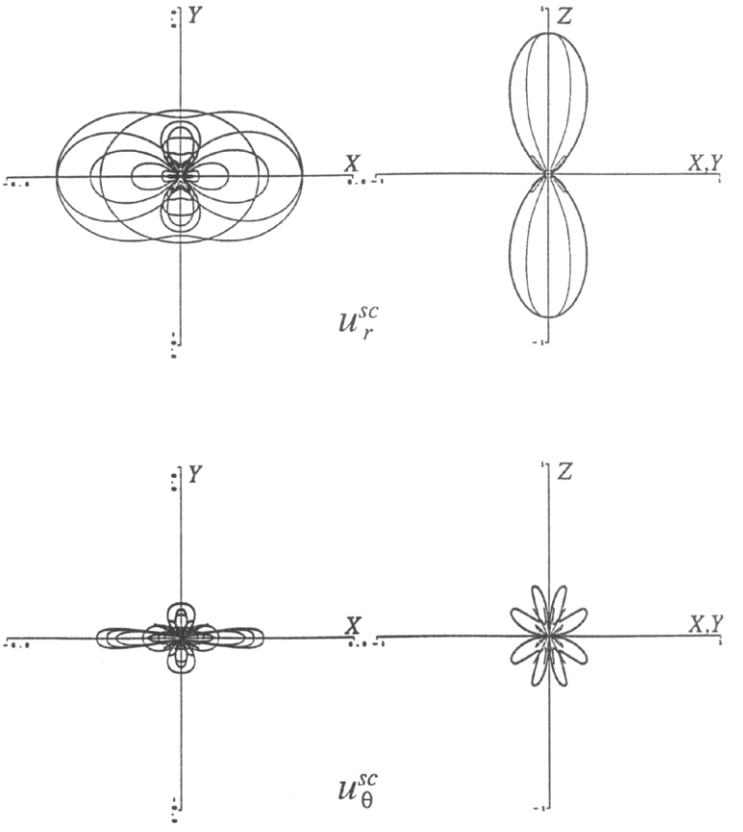

Fig. 15. Scattering patterns due to normal incidence, $\theta_0 = 0$, with $\overline{k_L} = \pi$, $\tau = 2$.

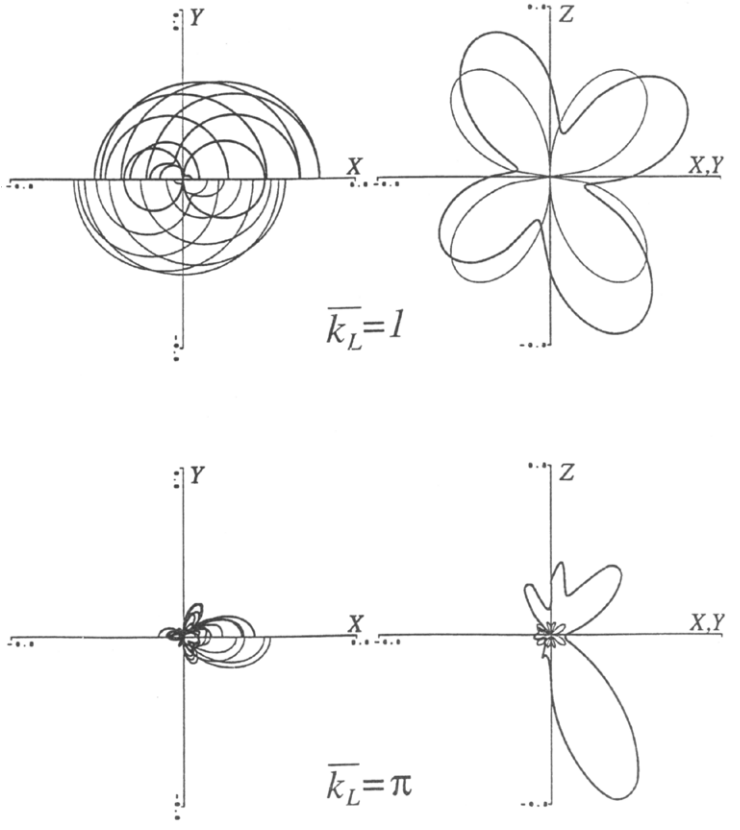

Fig. 16. Scattering patterns of u_θ^{sc} due to oblique incidence, $\theta_0 = 45^\circ$, $\tau = 1$.

is low, $\bar{k}_L = 1$ for instance. This illustrates the point that it is impossible to distinguish the *shape* of a crack based on low frequency scattered data.

At higher frequency, such as $\bar{k}_L = \pi$, the crack shape becomes visible in the longitudinal patterns observed from a direction normal to the crack face (Fig. 13), and the corner effects appear more clearly in the SV-wave patterns (Fig. 14). Because the corners are kinematically more stiff than the straight edges, it is expected that far less energy is scattered from the corners than from other parts of the crack edge. This effect is evident from Figs 13 and 14. Changing the aspect ratio to $\tau = 2$ (Fig. 15) further verifies this expectation since the lobes are much bigger on the longer-edge sides, comparatively smaller on the short-edge sides, and almost zero about the corner positions. This corner effect is a new feature of rectangular cracks in contrast with elliptical ones.

Finally, we note that the scattering patterns become much more complicated when the incidence is oblique (Fig. 16), especially in the high frequency region, and the aforementioned corner effect is difficult to discern. Nonetheless, at $\bar{k}_L = \pi$ the frequency is obviously high enough for the scattering patterns to show a ray character. Thus, the "reflected rays" in Fig. 16 are in the directions predicted by Snell's law (Achenbach, 1973).

REFERENCES

Achenbach, J. D. (1973). *Wave Propagation in Elastic Solids*. North-Holland, New York.

Achenbach, J. D., Gautesen, A. K. and McMaken, H. (1982). *Ray Method for Waves in Elastic Solids*. Pitman Advanced, Boston.

Bender, C. M. and Orszag, S. A. (1978). *Advanced Mathematical Methods for Scientists and Engineers*. McGraw-Hill, Maidenhead.

Budiansky, B. (1990). Private communication.

Budreck, D. E. and Achenbach, J. D. (1988). Scattering from three-dimensional planar cracks by the boundary integral equation method. *J. Appl. Mech., Trans. ASME* **55**, 405–412.

Bui, H. D. (1977). An integral equations method for solving the problem of a plane crack of arbitrary shape. *J. Mech. Phys. Solids* **25**, 29–39.

Gubernatis, J. E. and Domany, E. (1979). Rayleigh scattering of elastic waves from cracks. *J. Appl. Phys.* **50**(2), 818–824.

Itou, S. (1980). Dynamic stress concentration around a rectangular crack in an infinite elastic medium. *ZAMM* **60**, 317–322.

Krenk, S. and Schmidt, H. (1982). Elastic wave scattering by a circular crack. *Phil. Trans. R. Soc.* **A308**, 167–198.

Lin, W. and Keer, L. M. (1987). Scattering by a planar three-dimensional crack. *J. Acoust. Soc. Am.* **82**(4), 1442–1448.

Mastrojannis, E. N., Keer, L. M. and Mura, T. (1979). Stress intensity factor for a plane crack under normal pressure. *Int. J. Fract.* **15**(3), 247–258.

Nishimura, N. and Kobayashi, S. (1988). An improved boundary integral equation method for crack problems. In *Advanced Boundary Element Method* (Edited by T. A. Cruse), pp. 279–286. IUTAM, San Antonio, Texas.

Sih, G. C. and Liebowitz, H. (1968). Mathematical theories of brittle fracture. In *Fracture —an Advanced Treatise* (Edited by H. Liebowitz), Vol. II. Academic Press, New York.

Weaver, J. (1977). Three-dimensional crack analysis. *Int. J. Solids Structures* **13**, 321–330.